Analysis of Test Case Computations and Experiments for the First Aeroelastic Prediction Workshop

David M. Schuster[1], Jennifer Heeg [2], Carol Wieseman[3], and Pawel Chwalowski[4]
NASA Langley Research Center, Hampton, VA 23681

This paper compares computational and experimental data from the Aeroelastic Prediction Workshop (AePW) held in April 2012. This workshop was designed as a series of technical interchange meetings to assess the state of the art of computational methods for predicting unsteady flowfields and static and dynamic aeroelastic response. The goals are to provide an impartial forum to evaluate the effectiveness of existing computer codes and modeling techniques to simulate aeroelastic problems and to identify computational and experimental areas needing additional research and development. Three subject configurations were chosen from existing wind-tunnel data sets where there is pertinent experimental data available for comparison. Participant researchers analyzed one or more of the subject configurations, and results from all of these computations were compared at the workshop.

Nomenclature

C_p	=	Pressure coefficient
Re( )	=	Real component of the unsteady quantity, the component of the unsteady quantity that is in-phase with the wing motion.
Im( )	=	Imaginary component of the unsteady quantity, the component of the unsteady quantity that is 90° out-of-phase with the wing motion.
α	=	Angle-of-attack (°)
θ	=	Amplitude of pitch oscillation (°)
Δz	=	Amplitude of HIRENASD wing-tip displacement (mm)

I. Introduction

The Aeroelastic Prediction Workshop (AePW)[1] was patterned after two very successful workshops conducted over the past decade: the Drag Prediction Workshop[2] and the High Lift Prediction Workshop[3]. The AePW assembled an international slate of participants to analyze a carefully selected set of unsteady aerodynamics and aeroelastic problems for which experimental validation data is available. The intent of the workshop is to investigate the ability of present computational tools to predict nonlinear aeroelastic phenomena, particularly those arising from the formation of shock waves, vortices, and separated flow. A thorough description of the workshop formation and execution can be found in Reference 1.

In June 2011, the AePW was formally initiated at the International Forum on Aeroelasticity and Structural Dynamics held in Paris, France[4]. At this meeting, the objectives of the workshop and pertinent information required to participate in the event were provided to prospective analysts. A website was established (https://c3.nasa.gov/dashlink/projects/47/) where analysts and other interested parties could obtain participation information, modeling and analysis guidelines, test case data for the three configurations, experimental comparison data, computational grids, and other reference materials. This public site is still in operation today, and now contains a record of the analyses completed for the first AePW and future AePW plans. Computational grids for the three configurations were developed by the AePW Organizing Committee (OC) and distributed to the registered

[1] NASA Technical Fellow for Aerosciences, NASA Engineering and Safety Center, MS 431, Associate Fellow, AIAA.
[2] Senior Research Engineer, Aeroelasticity Branch, MS 340, and Senior Member, AIAA.
[3] Aerospace Engineer, Aeroelasticity Branch, MS 340, Associate Fellow, AIAA.
[4] Aerospace Engineer, Aeroelasticity Branch, MS 340, Senior Member, AIAA.

workshop participants. Participants analyzed the three workshop configurations for approximately nine months, submitting their results in March 2012. The AePW itself was held on April 21-22 in Honolulu, Hawaii, just prior to the AIAA 53rd Structures, Structural Dynamics, and Materials Conference. The workshop consisted of 59 registered attendees. A total of 17 analysis teams from 10 nations provided a total of 26 analysis datasets for evaluation.

The AePW OC selected three configurations for analysis by the participants:

1. Rectangular Supercritical Wing (RSW)[5-8]
2. Benchmark Supercritical Wing (BSCW)[9-11]
3. High Reynolds Number Aerostructural Dynamics Wing (HIRENASD)[12-18]

Each of these configurations will be briefly discussed here, but the reader is again directed to Reference 1 for a more complete description of the configuration selection process, each of the test case geometries, and the available data.

A. Rectangular Supercritical Wing

The Rectangular Supercritical Wing (RSW) was chosen to be the least complex, both geometrically and aerodynamically, of the three configurations for the AePW. The RSW was tested in the NASA Langley Transonic Dynamics Tunnel (TDT) in 1982, and a photograph from that test is shown in Figure 1. Figure 2 shows the geometric characteristics of the RSW. The wing is a simple rectangular planform with a wing tip of rotation. It has a span of 48 inches and a chord of 24 inches, with a 12%-thick supercritical airfoil section that is constant from wing root to tip. The wing was mounted to a relatively small splitter plate that was offset from the wind tunnel wall by approximately 6 inches. Unforced (steady) data were acquired with the model held at a fixed angle of attack. Dynamic data were acquired via forced oscillation of the model in pitch about the 46%-chord location. The wing was assumed to be rigid for all analyses.

This wing was originally chosen as an AePW configuration for its geometric simplicity and its transonic, but not overly challenging, aerodynamic characteristics. However, an unforeseen interaction of the wind tunnel wall with the airflow over the wing made this case significantly more difficult than anticipated. A calibration of the TDT**Error! Reference source not found.**, conducted after this test was performed, shows the wind-tunnel boundary layer for the wall on which the model and splitter plate were mounted to be approximately 12-inches thick at RSW test conditions of interest[19]. This places the RSW splitter plate well within the wind-tunnel wall boundary layer. The impact of this situation on the wing pressure distribution near the wing root was not appreciated by the AePW OC prior to the wing's selection as a workshop configuration. Preliminary AePW analyses of the RSW showed the inboard pressure distributions to be highly affected by the presence of the wind-tunnel wall boundary layer. The AePW organizers attempted to account for the wind-tunnel wall boundary layer and conducted extensive studies to characterize and correct models for this effect. These efforts are described in detail in Reference 20. Ultimately, the inclusion of the wind-tunnel wall

Figure 1: Rectangular Supercritical Wing mounted in the NASA Langley Transonic Dynamics Tunnel.

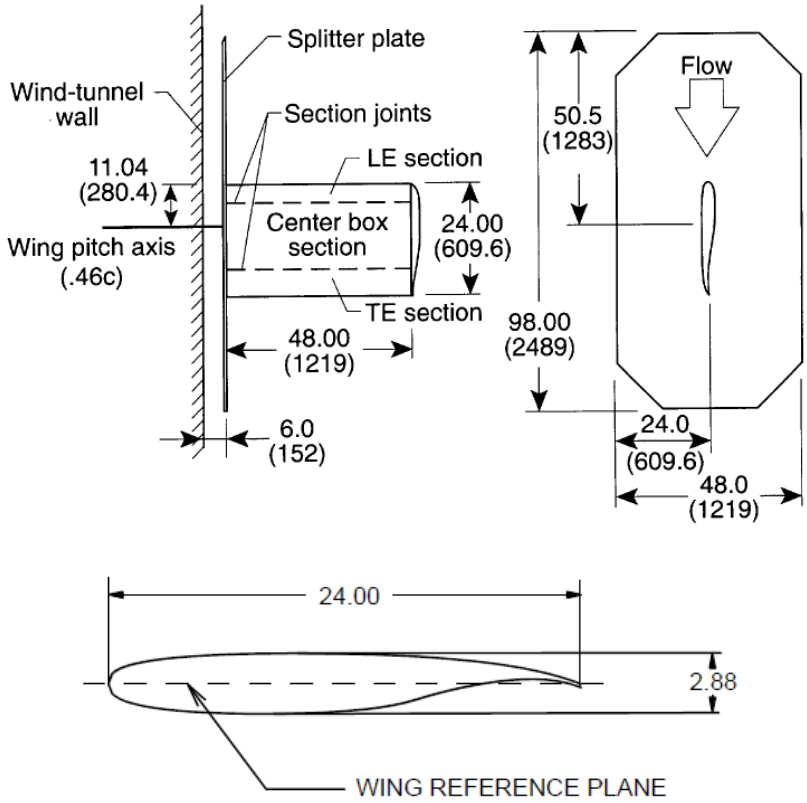

Figure 2: RSW geometric characteristics. Dimensions are shown in inches (mm).

boundary layer in the computational analyses made this case much more difficult than anticipated, resulting in significant deviations in comparisons between the CFD methods and the experimental data for the inboard pressure station.

The RSW was tested in R-12 heavy gas in the TDT, and all AePW analysts performed their simulations by changing the ratio of specific heats from $\gamma = 1.4$ to $\gamma = 1.132$ to account for the differences in thermodynamic properties between air and R-12. Experimental pressure data were measured at four constant-span stations on the wing: y/b = 0.308, 0.588, 0.809, and 0.951. These pressures included time-averaged pressure coefficients for the unforced data points and pressure coefficients processed at the frequency of the forced-pitch oscillation, in terms of magnitude and phase, for the dynamic data points. Reference 8 further post-processed the original magnitude and phase data into real (in-phase) and imaginary (90 degrees out-of-phase) pressure coefficient components scaled by the wing oscillation amplitude. There were no integrated force or moment measurements conducted in the test. Time history data from the test are no longer available.

The AePW OC chose a total of four test cases for analysis by the AePW participants, two unforced and two forced-oscillation. Table 1 shows the analysis conditions chosen for the RSW.

Table 1. Rectangular Supercritical Wing analysis conditions.

Mach Number	Mean Angle of Attack (α, deg.)	Pitch Oscillation Frequency (f, Hz)	Pitch Oscillation Amplitude (θ, deg.)	Reduced Frequency $\omega C/(2V_\infty)$	Reynolds Number (10^6/ft.)
0.825	2.0	0	0.0	0.0	2.0
0.825	4.0	0	0.0	0.0	2.0
0.825	2.0	10	1.0	0.152	2.0

0.825	2.0	20	1.0	0.304	2.0

B. Benchmark Supercritical Wing

The Benchmark Supercritical Wing (BSCW) configuration, shown in Figure 3 and Figure 4, has a geometric simplicity similar to the RSW, but it exhibited highly nonlinear unsteady behavior, specifically shock-separated transient flow. It was selected for the AePW to provide flow conditions that would prove more challenging for the analysts. While there are fewer pressure measurements than for the RSW configuration, the time history data records are available for all test conditions. In addition, the BSCW experimental data chosen for this case has not been widely published. It was obtained during check-out testing of the TDT Oscillating Turntable (OTT) hardware and thus was not the focus of a computational research project. While the data is publicly available in graphical form[11], it was viewed as obscure enough to serve as the basis for a semi-blind test case. Thus the experimental data was not provided to the AePW participants prior to the actual workshop.

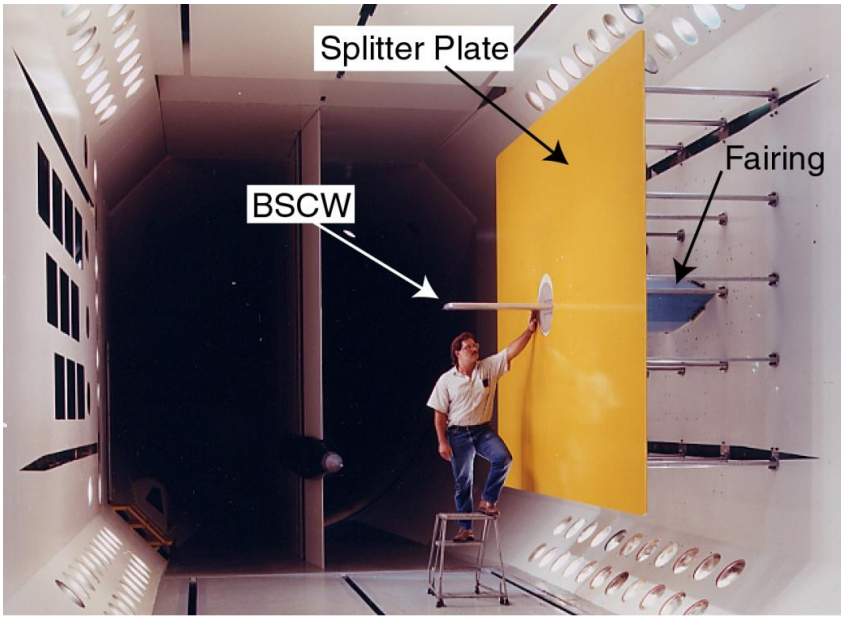

Figure 3: Benchmark Supercritical Wing mounted in the NASA Langley Transonic Dynamics Tunnel.

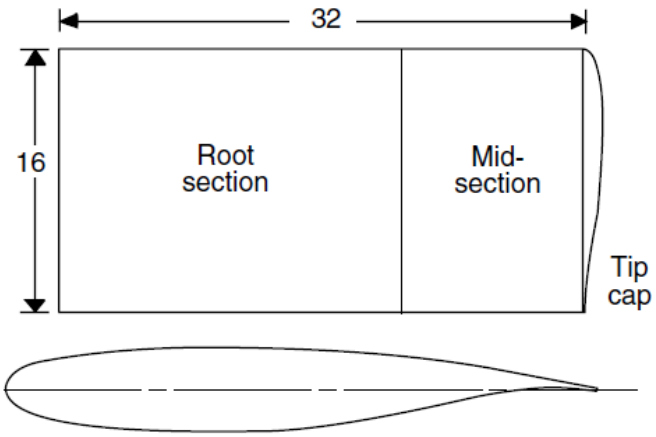

Figure 4: Planform and airfoil section for the Benchmark Supercritical Wing. Dimensions shown are in inches.

The BSCW has a rectangular planform with a NASA SC(2)-0414 airfoil. Like the RSW, the BSCW was tested in the TDT. However, the BSCW test was conducted after the TDT's conversion to R-134a as its heavy gas, so the cases for the BSCW were all computed with $\gamma = 1.116$ to account for this new test medium. The model was mounted to a large splitter plate that was offset from the TDT wall so as to place the wing closer to the center of the tunnel test section. This offset was well outside the wind tunnel wall boundary layer, so the BSCW avoided the issues with the wall boundary layer encountered on the RSW. The model's instrumentation is limited to one row of 40 in-situ unsteady pressure transducers at the 60% span station.

Dynamic data was obtained for the BSCW by oscillating the model in a pitching motion about the 30% chord. Unforced data at steady angle-of-attack was also acquired for this configuration and used for comparison with unforced simulations by the AePW participants. The analysis conditions chosen for the BSCW are shown in Table 2.

Table 2. Benchmark Supercritical Wing analysis conditions.

Mach Number	Mean Angle of Attack (α, deg.)	Pitch Oscillation Frequency (f, Hz)	Pitch Oscillation Amplitude (θ, deg.)	Reduced Frequency $\omega C/(2V_\infty)$	Reynolds Number (10^6/ft.)
0.85	5.0	0	0.0	0.0	3.4
0.85	5.0	1	1.0	0.01	3.4
0.85	5.0	10	1.0	0.10	3.4

C. High Reynolds Number Aerostructural Dynamics Wing

The High Reynolds Number Aerostructural Dynamics (HIRENASD) model was the final configuration chosen for analysis in the AePW. It was selected as an initial coupled aeroelastic analysis configuration. The wing has a high degree of structural stiffness and broad spacing of the structural modes, which produces weak aeroelastic coupling and makes it a good entry-level basis of evaluation. The additional benefits of this data set are availability of time histories and expertise from the experimentalists who are part of the AePW OC. Portions of the HIRENASD data set have been previously publicized, distributed, and analyzed[12-18].

HIRENASD was tested in the European Transonic Windtunnel (ETW) in 2007. The model, as installed in this facility, is shown in Figure 5, and described by References 12-14. It has a 34-degree aft-swept, tapered clean wing, with a BAC 3-11 supercritical airfoil profile. The test article is shown in Figure 6. It is a semi-span model, ceiling-mounted through a non-contacting fuselage fairing to a turntable, balance, and excitation system. The model and balance were designed to be very stiff, with well-separated modes. The first two wing bending modes have frequencies of approximately 27 and 79 Hz; the first wing torsion mode has a frequency of approximately 265 Hz. The model's instrumentation includes 259 in-situ unsteady pressure transducers at 7 span stations. Balance measurements and accelerations were also obtained. For a small set of data points, wing displacements were extracted via stereo pattern tracking.

Two types of testing were conducted for HIRENASD: angle-of-attack polars and forced oscillations. The angle-of-attack polar data was obtained by slowly varying the angle of attack at an angular sweep rate of 0.2 degrees/second, holding all other operational parameters constant. These data were utilized primarily to provide static pressure distributions at a given test condition. The forced-oscillation data was obtained by differential forcing at a specified modal frequency. All forced-oscillation data used in the AePW was excited near the wing's second bending modal frequency. Forced-oscillation fluctuating pressure data was referenced to the response of an accelerometer mounted in the wind tunnel model near the wing tip, designated as accelerometer 15 by the HIRENASD test team.

Analysis of the unforced data by the AePW OC found the polar data to be somewhat inconsistent from run to run, possibly owing to the continuous sweep approach to acquiring the data. Experimental data was also acquired in the "rest periods" between the forced-oscillation runs, and the AePW OC felt these data showed better run-to-run consistency and also served as a better unforced initial condition for the forced-oscillation computations. Therefore, the unforced data from the rest periods between forced oscillation tests were used for the steady experimental data supplied to the AePW participants.

Two Reynolds numbers, 7.0 million and 23.5 million based on reference chord, were analyzed by the AePW participants. Test cases were chosen at two Mach numbers, 0.70 and 0.80. The lower Reynolds number case has an angle of attack of 1.5 degrees, while a more challenging angle of attack of -1.34 degrees, corresponding to the zero-

Figure 5: HIRENASD wing mounted in the European Transonic Windtunnel.

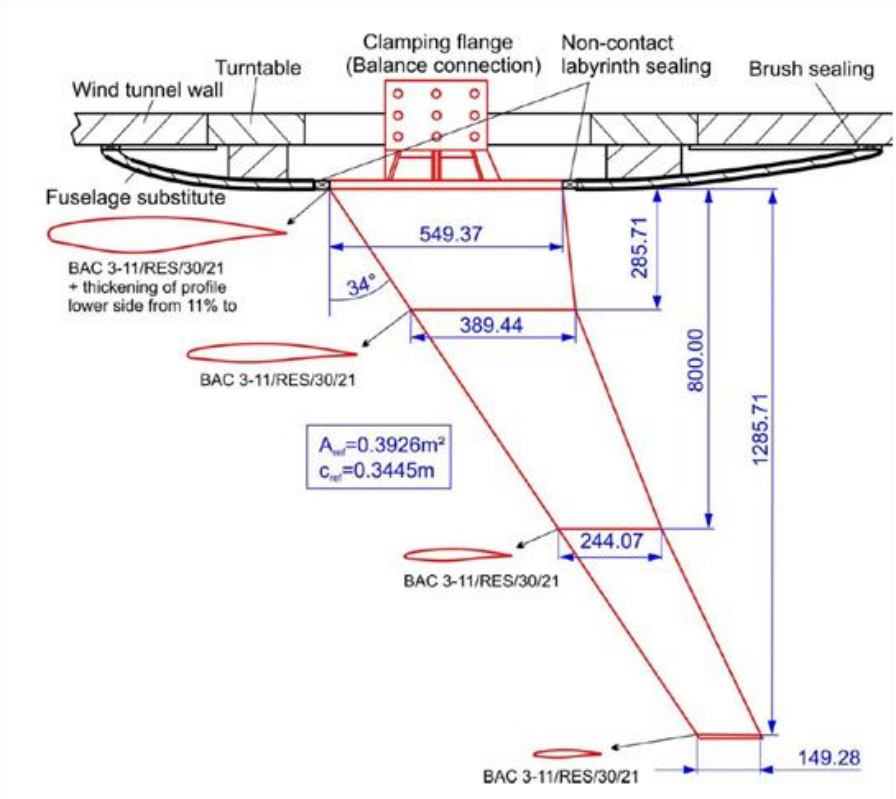

Figure 6: HIRENASD wing planform, dimensions in mm unless otherwise noted.

lift condition, was selected for analysis at the higher Reynolds number. At Mach 0.7, only the lower Reynolds number data were analyzed. This condition was selected as a simpler case with no appreciable aerodynamic nonlinearity. Both the low and high Reynolds numbers were computed at the more challenging 0.80 Mach number. All tests were conducted with nitrogen ($\gamma = 1.4$) as the test medium.

Analysis conditions chosen for the HIRENASD wing are shown in Table 3.

Table 3. HIRENASD analysis conditions.

Mach Number	Mean Angle of Attack (α, deg.)	Forcing Frequency (f, Hz)	2nd Bending Amplitude (Δz, mm)	Reduced Frequency $\omega C/(2V_\infty)$	Chord Reynolds Number ($*10^6$)
0.70	1.5	0	0.0	0.0	7.0
0.80	1.5	0	0.0	0.0	7.0
0.80	-1.34	0	0.0	0.0	23.5
0.70	1.5	79.3	2.0	0.378	7.0
0.80	1.5	78.9	2.4	0.333	7.0
0.80	-1.34	80.4	0.9	0.396	23.5

D. Workshop Data

Comparison of unforced and forced-oscillation pressure coefficient data for each of the three configurations is the primary focus of this paper. Integrated loads data for each of the configurations was collected from the analysts as well, but only the HIRENASD test measured forces and moments experimentally. For the unforced cases, the pressure coefficient is compared with experimental data at select span stations on each wing. For the forced-oscillation cases, the frequency response of the fluctuating pressure coefficient time histories are computed at the wing excitation frequency, and the real and imaginary components of the response function are compared with corresponding experimental data. The forced-oscillation pressure coefficient is normalized by the wing oscillation amplitude (in degrees) for the RSW and BSCW pitch oscillation cases and by the tip deflection (in millimeters) for the HIRENASD cases. In the present nomenclature, the real part of the fluctuating pressure coefficient is that component which is in phase with the wing motion, while the imaginary part is the component that is ninety degrees out of phase with the motion.

Depending on the configuration, between 6 and 14 analysts performed computations on each case. This paper examines all submissions for a particular case as a whole and does not try to split out variations in computational algorithm, grid refinement, turbulence modeling, or temporal refinement. A sample of available computational data for the RSW is shown in

Figure 7. Figure 7a shows the pressure distributions from all of the analysts who computed the M = 0.825, α = 2.0° unforced case at the $\eta = 0.309$ span station. In this figure, all of the analysts' computations are depicted with identical solid lines, with no distinction between individual analysts, computational algorithm, grid refinement, turbulence model, or other distinguishing feature between the computations. The plot represents the total variation in the predictions of the case at this station from all of the AePW submissions. To simplify the display of the data and facilitate further analysis, the submitted data was processed to compute an average pressure distribution from all the analyst submissions, along with an envelope around the average that encompasses all of the predictions, as shown in Figure 7b. In this figure, the solid lines represent the upper surface pressure distribution, and the dashed lines depict the lower surface pressures. In each, the dark line is the mean of all the submissions, and the lighter lines are the envelope around the mean. This approach provides a less cluttered summary of the CFD performance for this case, distinctly showing where the methods consistently predict similar behavior and where they differ. In some cases, the dark mean line may be biased to one side of the envelope. This indicates that for this situation, the majority of the simulations favored the near side of the envelope, while the far side of the envelope was predicted by a minority of the simulations. Biases of this type will be pointed out in the discussion of the data when they occur. For instance, in

Figure 7b, the mean upper surface pressure distribution near 80% chord strongly favors the more negative side of the envelope, indicating that most of the computations were clustered in this vicinity. This technique will be used throughout the remainder of this paper to discuss and analyze the performance of the CFD methods and how they compare with experimental data.

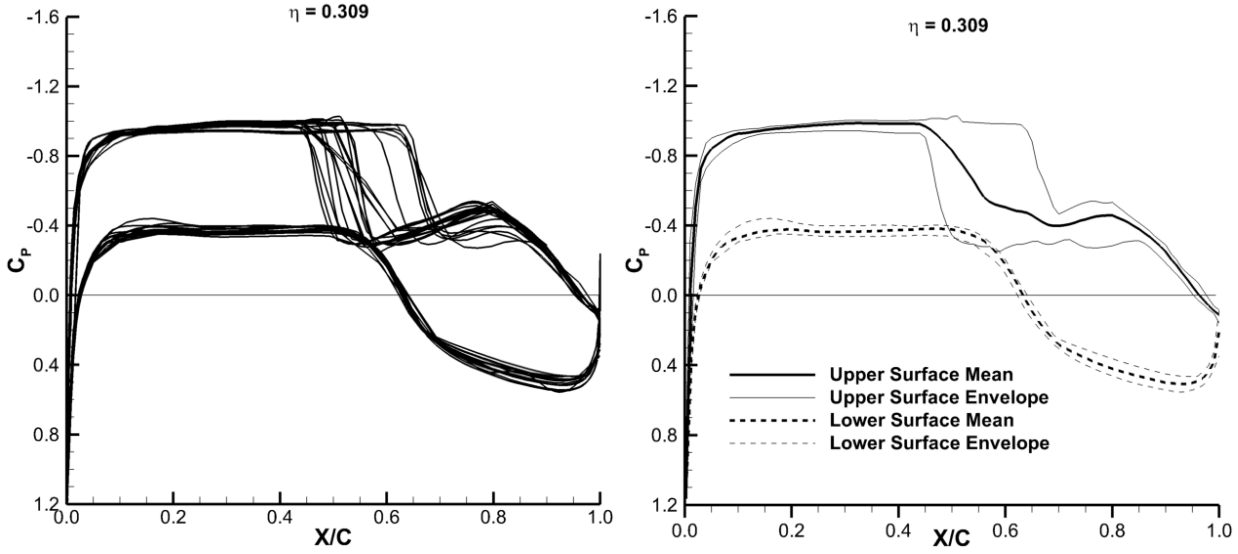

a) All analysts' computations.

b) Average pressure distribution with surrounding envelope pressure.

Figure 7. Pressure distribution enveloping technique used in data analysis, RSW M = 0.825, α = 2.0°,θ = 0.0°, f = 0 Hz.

II. AePW Data Analysis

A. Rectangular Supercritical Wing

Six analysts provided results for the RSW using a variety of computational algorithms and grid refinement. For the unforced cases, all did a coarse/medium/fine grid convergence study, and most did the same for the forced-oscillation cases. Some of the analysts provided temporal convergence studies for the forced-oscillation cases as well. All computations solved the Reynolds-Averaged Navier-Stokes (RANS) equations using both structured and unstructured grid formulations. For the RSW, all of the analysts used some form of the Spalart-Allmaras turbulence model except for one, who used the Menter Shear Stress Turbulence (SST) model. Reference 20 provides a high degree of technical detail for both the experimental and computational analyses performed on this case,

The unforced cases will be discussed first, beginning with the M = 0.825, α = 2.0° case. The computed pressure distributions at the η = 0.309 and 0.809 stations are compared with experimental data in Figure 8a and b, respectively. The computations predict consistent results, with the exception of the aft upper surface on the inboard wing station. The predicted location of the upper surface shock varies widely at the inboard span station with a total variation in shock location of approximately 20% chord. At this station, the results can generally be grouped into two distinct sets, those predicting a forward shock at approximately 50% chord near one side of the envelope around the mean pressure, and those with an aft shock near 65% chord near the other side of the envelope. The majority of the simulations predicted the forward shock location, as shown by the bias of the mean toward the left side of the envelope near 50% chord. One set of data exhibiting the aft shock location modeled the wing from the splitter plate outboard, with an inviscid wind-tunnel wall. This explains the aft shock location predicted for these cases as demonstrated in Reference 20. However, some of the aft shock cases did model the problem with the viscous wind-tunnel wall. An examination of the variation of shock location with grid resolution showed that none of the analysts predicted a shift in the shock location that went from the aft shock position to the forward position as a result of improved grid refinement. Most of the computations predict the shock on the outboard station slightly aft of the experiment, but the calculations only vary in location by about 5% chord. On the wing lower surface, the computed

pressures at both span stations are very consistent and compare favorably with the experimental data everywhere except aft of about 70% chord. This is in the reflexed cove region of the supercritical airfoil section, and it is not clear what may be contributing to these differences. The pressure magnitude is over-predicted by all of the CFD methods. The outboard wing station is farther away from the area of the wing that was immersed in the wind-

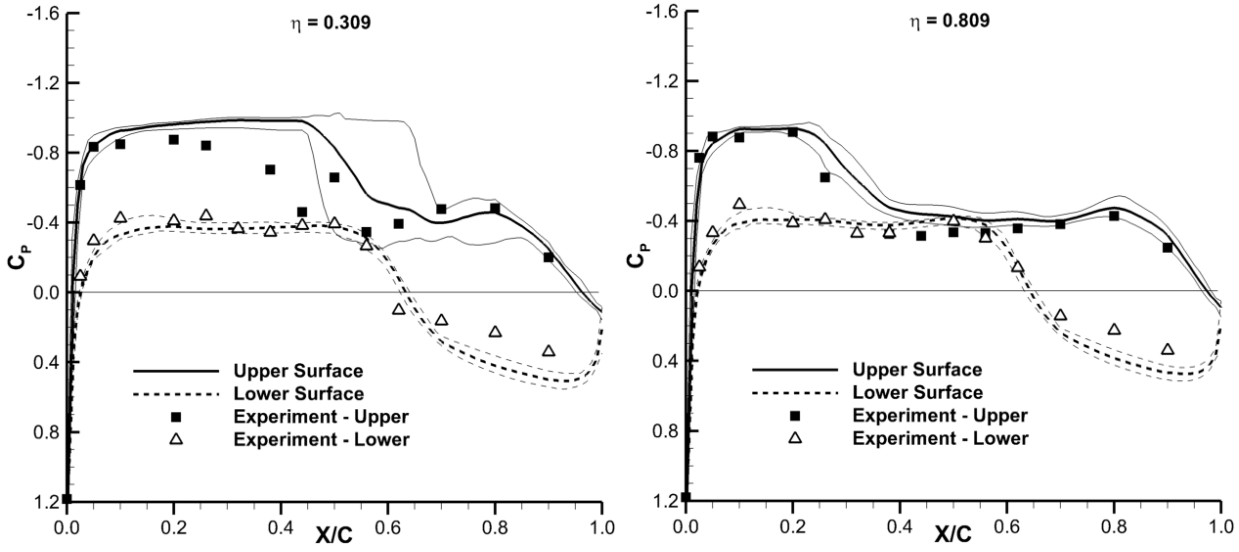

a) Inboard wing station. b) Outboard wing station.

Figure 8. RSW unforced pressure comparison, M = 0.825, α = 2°, θ = 0.0°, f = 0 Hz.

tunnel-wall boundary layer, and the computations and experimental data appear to be less susceptible to this problem here.

A similar set of results are presented for the α = 4° case in Figure 9. Again, at the inboard station, the predicted shock locations vary widely among the computations, with a total spread of approximately 18% chord. Forward of the shock on the upper surface, and across the entire lower surface, all of the computations predict very consistent results and compare reasonably well with the experimental data. On the outboard station, most of the computations predict a shock location slightly aft of the experiment, with a total variation among the predictions of less than 5% chord. The lower surface pressures in the cove region of the wing are again consistently over-predicted by the computations.

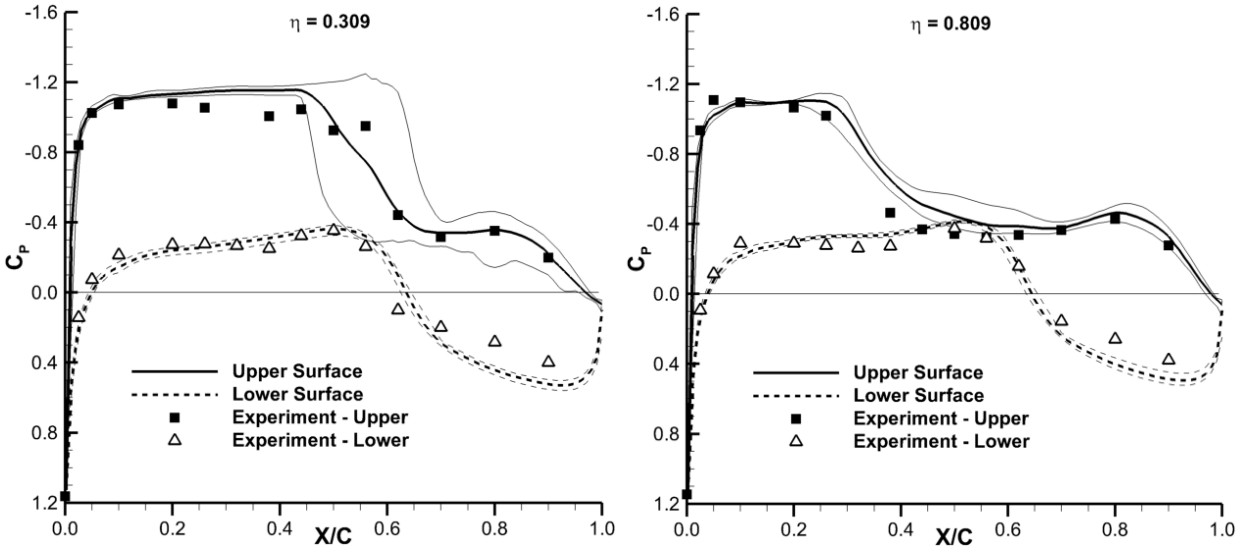

a) Inboard wing station. b) Outboard wing station.

Figure 9. RSW unforced pressure comparison, M = 0.825, α = 4°, θ = 0.0°, f = 0 Hz.

For the forced-oscillation analyses, the RSW was oscillated in pitch about a steady angle attack of α = 2° with an amplitude of θ = 1°. Two frequencies were investigated, 10 and 20 Hz. Table 4 summarizes the parameters used by each of the analysts for the 10 Hz forced-oscillation case. On the far left of the table, individual analyst teams are designated by the letters A-F. The center table section designates the level of grid refinement, coarse (C), medium (M), or fine (F), the time step employed in terms of time steps per cycle of motion, the number of cycles of motion computed, and the number of subiterations between time steps. The right side of the table provides derived physical properties of the parameter choices important to the temporal processing of the computed data. Figure 10 compares the computed and experimental forced-oscillation pressure distributions for the f = 10 Hz case. Figure 10a and 10b compare results for the η = 0.309 station, while Figure 10c and 10d compare data at the η = 0.809 station. The real (in-phase) pressure coefficient is shown on the left while the imaginary (out-of-phase) components are shown on the right. At both the inboard and outboard stations, the lower surface fluctuating pressure calculations show good consistency across the various analyses and generally compare favorably with the experimental data. The exception to this is the envelope near the lower surface leading edge on the inboard station. In this area, one of the analyses exhibited some apparent local stability problems that expanded the pressure envelope in this region. The upper surface calculations show good consistency and comparison with the experimental data, with envelopes expanding in the vicinity of and behind the moving shock wave. The expansion of the envelope is large on the inboard station, due to the influence of the wind-tunnel-wall boundary layer at this station. The experimental data in this region shows the real component of pressure to have a slightly greater proportion of the unsteady pressure than the imaginary component, with the real component peaking at a magnitude of nearly 0.3 (-0.3 true value), while the imaginary component peaks at a magnitude of nearly 0.15. This indicates that at this frequency the peak fluctuating pressure coefficient generated by the moving shock is closer to being in-phase with the pitching motion than 90° out-of phase with the motion. The opposite trend is observed at the higher frequency, to be discussed subsequently. On the outboard station, the mean of the computations do not seem to capture this feature with the real component of the peak fluctuating pressure at the shock near -0.2 and the imaginary peak near +0.2, thus with similar peak magnitude. However, with the large envelope surrounding the computations, it is impossible to make a general conclusion about the ability of individual computations to predict this trend.

Table 4. RSW time accurate computation parameters, f = 10 Hz.

Analyst Team	Grid Res	# of Steps per Cycle	# of Cycles Computed	# of Subiters per Global Time Step	Time Record Length (sec)	Nyquist Frequency (Hz)	Fourier Frequency Resolution (Hz)
A	M	64	7	Variable	0.7	320	1.43
B	C	[64, 256]	8	25	0.8	[320. 1280]	1.25
	M	64	8	25	0.8	320	1.25
	F	[64, 1024]	[8, 4]	25	[0.8, 0.4]	[320, 5120]	[1.25, 2.50]
C	M	[200, 400, 800]	[6, 12, 3]	4	[0.6, 1.2, 0.3]	[1000, 2000, 4000]	[1.67, 0.84, 3.34]
D	C	[32, 64, 128]	5	[15, 10, 7]	0.5	[160, 320, 640]	2.00
	M	[32, 64, 128]	5	[18, 11, 8]	0.5	[160, 320, 640]	2.00
	F	64	4	14	0.4	320	2.50
E	C	64	5	50	0.5	320	2.00
	M	64	5	50	0.5	320	2.00
F	C	64	6	50	0.6	320	1.67
	M	64	6	50	0.6	320	1.67

The unforced simulations indicated that some of the analysts predicted a steady shock location near 65% chord, while a larger proportion of analysts predicted the location closer to 50% chord. It is likely that this difference in

shock location from the unforced simulations accounts for the double-lobed distribution in the upper surface envelope for this forced-oscillation case. At the inboard station, the envelope of the computations generally contains the experimental data. On the outboard station, away from the influence of the wind-tunnel-wall boundary layer, the computations show much smaller variation in the vicinity of the upper surface shock centered at approximately 25% chord. However, none of the methods predict the peak real-component amplitude in this region, and only the edge of the computational envelope captures the peak imaginary component amplitude here. Behind the shock on both the inboard and outboard stations, the pressure envelope of the computations spreads as compared to the envelope ahead of the shock. This indicates increased variation in the prediction of the shock/boundary layer interaction and the influence of the prediction of this interaction on the downstream pressure distribution.

Table 5 provides a summary of the parameters used in the time accurate analyses for the f = 20 Hz case, similar to those previously provided in Table 4. For the most part, the analysts chose to analyze the f = 20 Hz case with temporal parameter selections that are very similar to those used for the f = 10 Hz case. This results in generally higher Nyquist frequency values and poorer Fourier frequency resolution for the f = 20 Hz simulations. Figure 11 presents fluctuating pressure comparisons for this case. The majority of the peak fluctuating pressure due to the shock motion at the inboard station is 90° out-of-phase with the wing pitch motion, as indicated by the increased

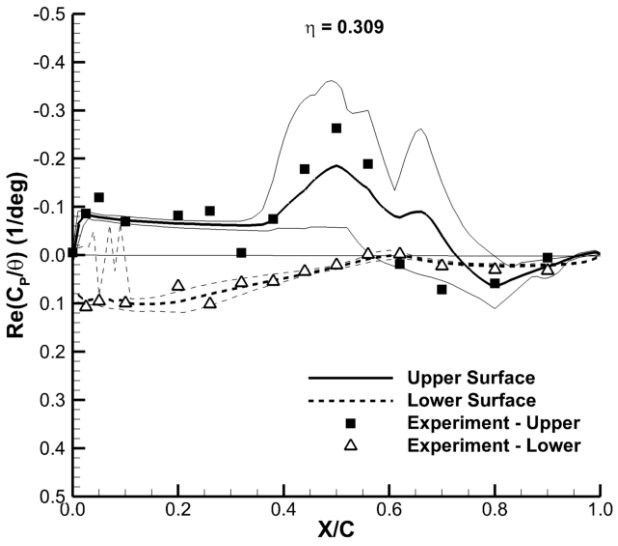

a) Real component, inboard wing station.

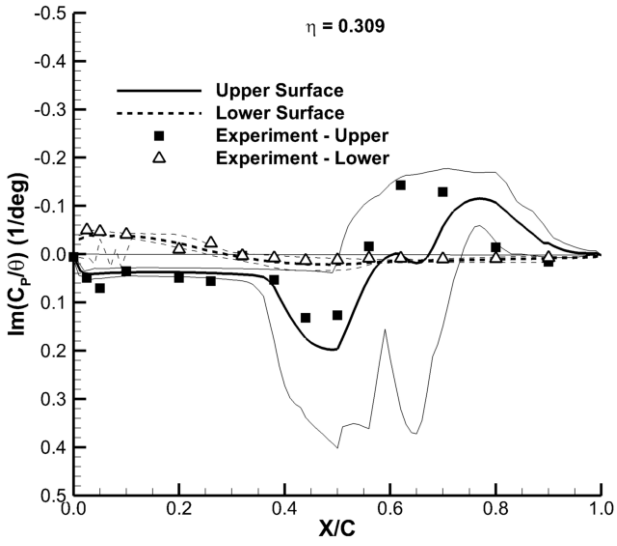

b) Imaginary component, inboard wing station.

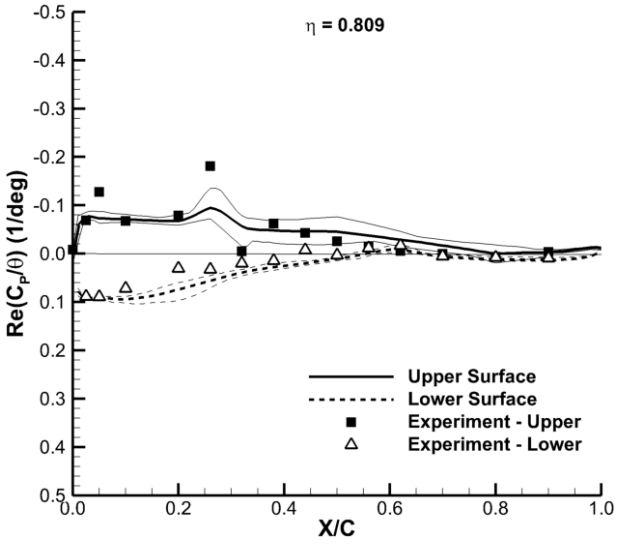

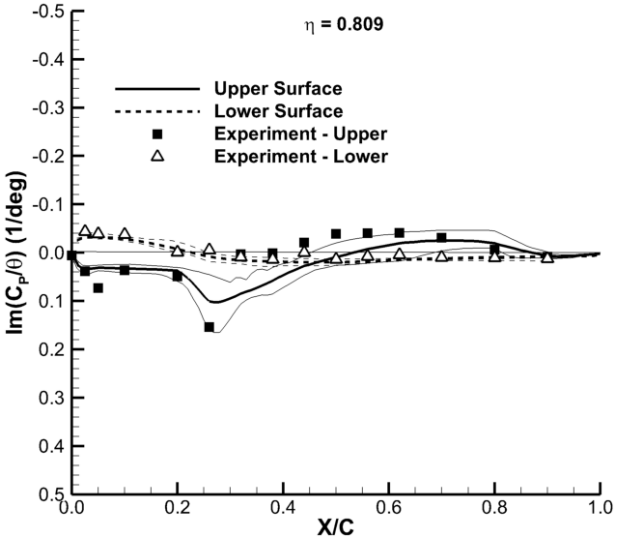

c) Real component, outboard wing station. d) Imaginary component, outboard wing station.

Figure 10. RSW unsteady pressure comparison, M = 0.825, α = 2°, θ = 1.0°, f = 10 Hz.

Table 5. RSW time accurate computation parameters, f = 20 Hz.

Analyst Team	Grid Res	# of Steps per Cycle	# of Cycles Computed	# of Subiters per Global Time Step	Time Record Length (sec)	Nyquist Frequency (Hz)	Fourier Frequency Resolution (Hz)
A	M	64	6	Variable	0.3	640	3.33
B	C	128	8	25	0.4	640	2.5
	M	128	5	25	0.25	1280	4.0
	F	[128, 1024]	[5, 2]	25	[0.25, 0.1]	[1280, 10240]	[4.0, 10.0]
C	M	[200, 400, 800]	[6, 6, 3]	4	[0.3, 0.3, 0.15]	[1000, 2000, 4000]	[3.35, 3.35, 6.7]
D	C	[32, 64, 128]	5	[13, 9, 6]	0.25	[320, 640, 1280]	4.0
	M	64	5	9	0.25	640	4.0
E	C	64	5	50	0.4	640	2.5
	M	64	5	50	0.4	640	2.5
F	C	64	6	50	0.3	640	3.33
	M	64	6	50	0.3	640	3.33

amplitude of the imaginary component of the pressures at approximately 50% chord. The general character of the computed pressures is similar to that of the f = 10 Hz case, with the variation across the methods small on the lower surface and ahead of the shock and the variation expanding near and aft of the shock. Comparisons with the experimental data on the outboard wing station and on the inboard station lower surface and upper surface forward of the shock can be classified as good. Near and aft of the shock on the inboard station upper surface, the experimental pressures are enveloped by the computations, but the variation in the computed data is large, due again to the interaction with the wind-tunnel-wall boundary layer in this region.

B. Benchmark Supercritical Wing

The Benchmark Supercritical Wing (BSCW) was chosen because it has a simple wing planform, there is recent comprehensive unsteady experimental data available, and these data exhibit some strong nonlinear aerodynamic phenomena. In addition, these recent data have not been widely published making the BSCW a semi-blind test case for the AePW participants. The test case was centered on a single Mach number/angle of attack combination, with M = 0.85 and α = 5.0°, as previously shown in Table 2. AePW participants were not supplied with the experimental data prior to performing their computations. Each analyst first performed a set of computations at a constant angle of attack to provide an initial condition for the forced pitch-oscillation simulation. The results of these constant angle-of-attack computations at the 60% wing span station are shown in Figure 12. As with the RSW case, the BSCW computations show very little variation among the participants across the lower surface of the wing and on the upper surface forward of the predicted shock location. On the upper surface, the computations compare very favorably with the experimental data up to approximately 45% chord. Complete time histories are available for this set of experimental data, and observed maximum and minimum pressures at each of the transducer locations can be extracted from the pressure time history data. At approximately 45% chord, the experimental data indicates a large increase in the difference between the maximum and minimum pressure coefficient, which is indicative of unsteady shock motion. The pressure transducers located at the 40% and 50% chord locations show a much smaller difference between the maximum and minimum pressures, suggesting that the shock oscillation is confined to the region between these two sensors. The large majority of the computations predict a shock location of between 50 and 60% chord, somewhat aft of this point. The shock location varies approximately 10% chord across all the participants, with the mean position at about 53% chord. The majority of the methods also predict similar post shock behavior, though at an elevated pressure from the experiment. On the lower surface, the computations produce very consistent results up to the shock, and like the RSW case, they tend to over-predict the pressures in the cove region

of the supercritical airfoil. The computed differences in the lower surface shock location are not as widespread as on the upper surface.

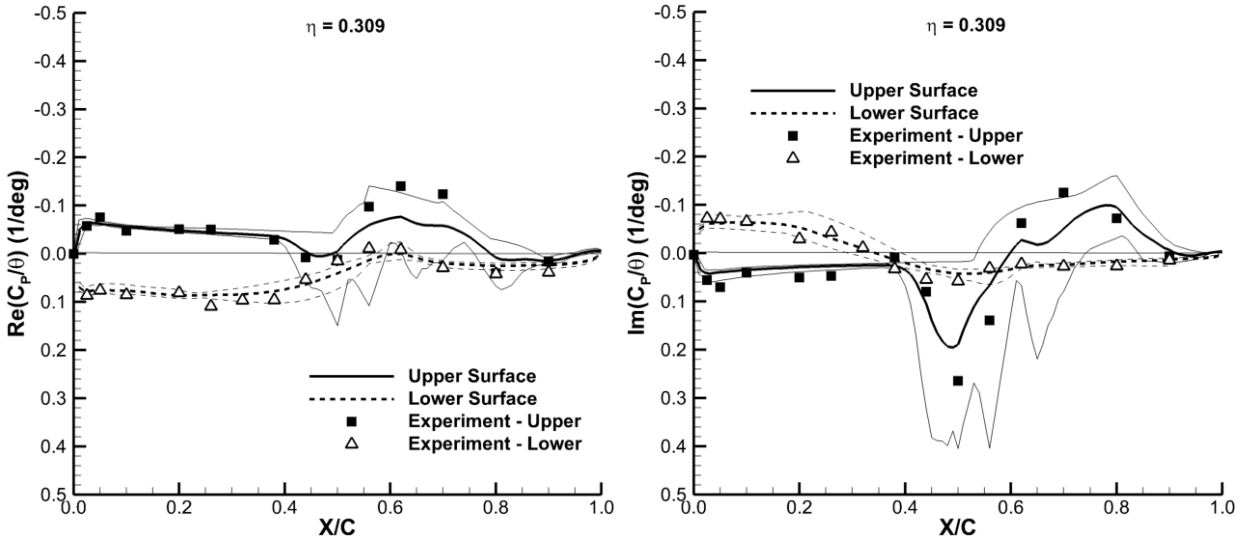

a) Real component, inboard wing station. b) Imaginary component, inboard wing station.

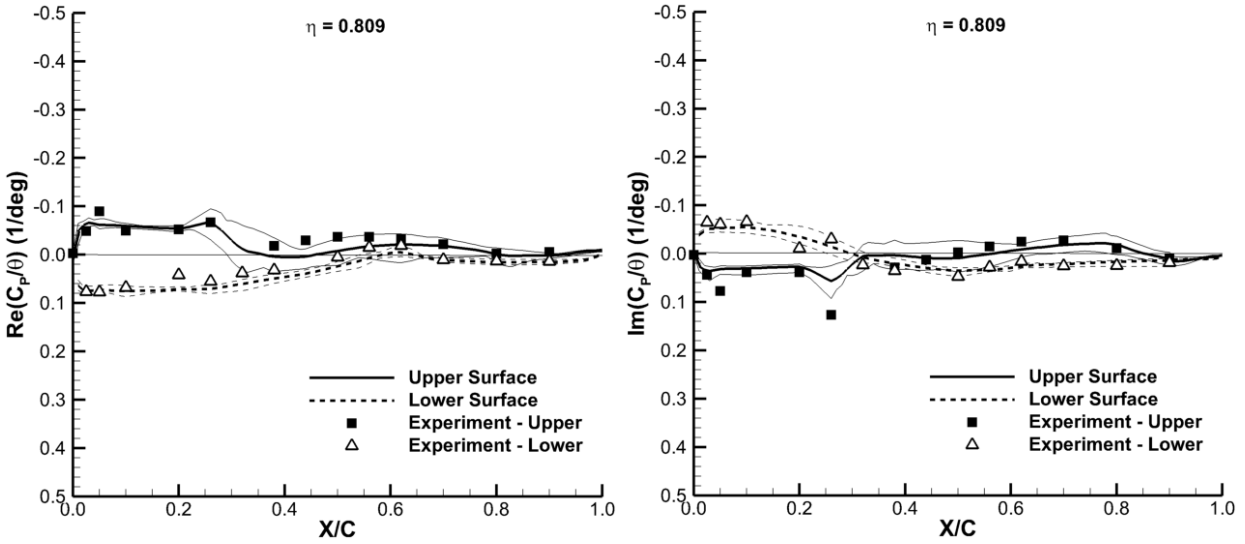

c) Real component, outboard wing station. d) Imaginary component, outboard wing station.

Figure 11. RSW unsteady pressure comparison, M = 0.825, α = 2°, θ = 1.0°, f = 20 Hz.

The AePW analysts indicated that the static angle-of-attack simulations produced a mixture of steady and unsteady flow. Many of the coarse grid simulations converged to a steady state, while as the grid was refined to the finer grids, the unforced solutions became unsteady. Upper surface shock-induced boundary-layer separation is believed to be the root cause for this unsteadiness in the unforced data. This required many of the analysts to employ an unsteady CFD analysis of the unforced case, as opposed to a steady-state simulation. The unsteadiness in the static angle-of-attack data and the varied approaches of the AePW analysts to simulate this problem are what likely lead to the wide variation in prediction of the shock location on the upper surface of the wing.

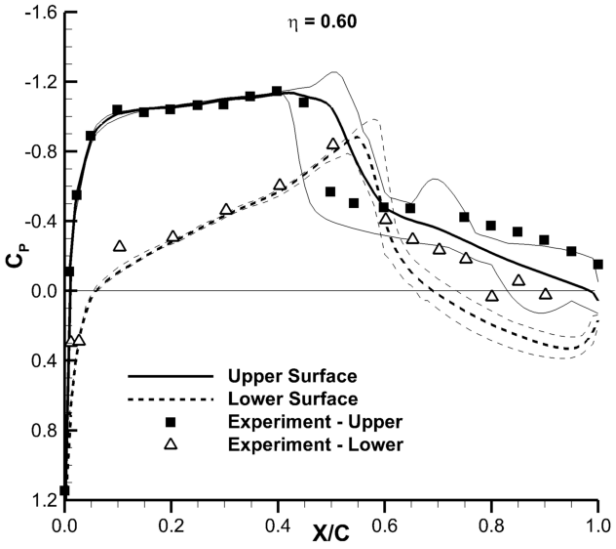

Figure 12. BSCW steady pressure comparison, M = 0.85, α = 5°, θ = 0.0°, *f* = 0 Hz, η = 0.60.

Two forced pitch-oscillation cases were investigated, one at a relatively low frequency of *f* = 1 Hz and the second at *f* = 10 Hz, both with an oscillating pitch amplitude of θ = 1° and a mean angle-of-attack of α = 5°. Table 6 provides the parameters used by each of the BSCW analysis teams to conduct the *f* = 1 Hz forced-oscillation simulations. The real and imaginary components of the computed pressure coefficient for the 1 Hz frequency case are compared to the experimental data in Figure 13. The mean real component of the computed data shows an upper surface shock peak at approximately 54% chord, which is well aft of the experimental peak at about 45% chord. The mean of the computed data is also lower in peak amplitude at the upper surface shock location. It is difficult to tell exactly where the experimental peak occurs since it is unlikely that there is a pressure sensor located precisely at the shock location. In this case, it can be inferred from the shape of the pressure distribution that the shock peak occurs somewhere between 45% and 50% chord. Away from the upper surface shock, the real component compares very well with the experimental data, including a close prediction of the lower surface shock position and oscillating pressure amplitude. The experimental data shows the forced pitch-oscillation pressure distribution responds in near perfect phase with the wing motion, as evidenced by the very flat, near-zero imaginary component of the pressure coefficient. The mean of the computed data follows this trend closely, with only small out-of-phase components predicted near the upper and lower surface shock locations.

Table 6. BSCW time accurate computation parameters, *f* = 1 Hz.

Analyst Team	Grid Res	# of Steps per Cycle	# of Cycles Computed	# of Subiters per Global Time Step	Time Record Length (sec)	Nyquist Frequency (Hz)	Fourier Frequency Resolution (Hz)
A	M	128	5	Variable	5	64	0.20
B	C	128	8	25	8	64	0.13
	M	[128, 256, 1024]	[8, 4, 2]	25	[8, 4, 2]	[64, 128, 512]	[0.13, 0.25, 0.50]
	F	[128, 1024]	[8, 2]	25	[8, 2]	[64, 512]	[0.13, 0.50]
C	M	[200, 400, 800]	[9, 9, 3]	[6, 4, 4]	[9, 9, 3]	[100, 200, 400]	[0.11, 0.11, 0.33]
D	C	[180, 360, 720, 720]	4	[20, 20, 20, 50]	4	[90, 180, 360, 360]	0.25
	M	720	4	50	4	360	0.25
F	C	200	10	20	10	100	0.10
	M	200	10	20	10	100	0.10
	F	200	10	20	10	100	0.10

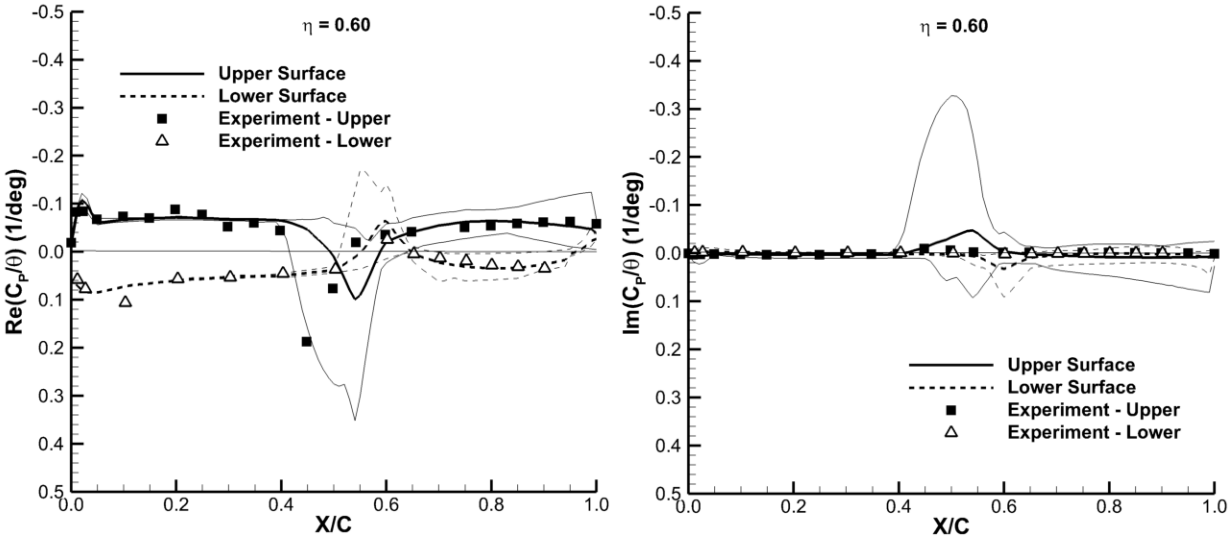

a) Real component. b) Imaginary component.

Figure 13. BSCW unsteady pressure comparison, M = 0.85, α = 5°, θ = 1.0°, f = 1 Hz, η = 0.60.

The temporal parameters used by each of the BSCW analysis teams to compute the f = 10 Hz case are shown in Table 7. As with RSW, the choices of parameters between the two different frequency computations are very similar. The fluctuating pressure results for this case are shown in Figure 14. Again, it appears that the majority of the AePW analysts are predicting a shock location aft of the experiment on the upper surface. Like the 1 Hz case, the real component of pressure near the upper surface shock is lower in amplitude and aft of the experimental peak. On the lower surface, the mean of the computations shows good agreement with the experimental data everywhere, including the position and amplitude of the shock peak. For this higher frequency case, the experimental data shows a larger imaginary component of pressure response, particularly near the upper surface shock. Again, the mean of the computations show a shock location that is aft of the experimental peak, but the peak amplitude is close to the experimentally measured values. It is reiterated that it is impossible to determine the precise location and magnitude of the experimental peak due to the likelihood that a pressure sensor is not located on the peak. Away from the upper surface shock, the overall character of the out-of-phase pressure component compares very well with the experimental data.

C. HIRENASD

The data selected for the HIRENASD configuration investigated the unforced and forced aerodynamic response to changes in Mach number and Reynolds number. Mean and fluctuating pressures were compared at M = 0.70 and M = 0.80 at α = 1.5° and 7 million Reynolds number based on the wing reference chord. A higher Reynolds number case of 23.5 million at M = 0.80 and α = -1.34° was also investigated. Unlike previous cases where the wing was oscillated in pitch, the forced motion for HIRENASD was generated by exciting the wing second-bending mode near its natural structural frequency of 79 Hz. The span stations shown for comparison in the following figures were chosen to be near the anti-node of the second-bending mode, where the wing deformation would be largest. Since the model was effectively clamped at the wing root, the deformation at the inboard anti-node will be smaller than the deformation at the outboard station. The fluctuating pressure response is scaled by the maximum deflection of the wing measured at a point near the wing tip. This deflection, along with the frequency of oscillation, is listed in Table 3 for the three forced-oscillation test cases. AePW analysts chose to model the modal excitation in one of two ways: (1) specified motion of the second bending mode with a prescribed frequency and amplitude, or (2) through a fully aeroelastic simulation, where the structural dynamics equations of motion are coupled with the aerodynamics and the model anchor point is oscillated similar to the approach used in the wind-tunnel testing. Results from both approaches are included in the forced-oscillation pressure comparisons presented below and no attempt is made to investigate result differences due to these varied approaches.

Table 7. BSCW time accurate computation parameters, f = 10 Hz.

Analyst Team	Grid Res	# of Steps per Cycle	# of Cycles Computed	# of Subiters per Global Time Step	Time Record Length (sec)	Nyquist Frequency (Hz)	Fourier Frequency Resolution (Hz)
A	M	64	6	Variable	0.6	320	1.67
B	C	128	8	25	0.8	640	1.25
	M	[128, 1024]	[8, 2]	25	[0.8, 0.2]	[640, 5120]	[1.25, 5.0]
	F	[128, 1024]	[4, 2]	25	[0.4, 0.2]	[640, 5120]	[2.5, 5.0]
C	M	[200, 400, 800]	[9, 9, 3]	[4, 4, 4]	[0.9, 0.9, 0.3]	[1000, 2000, 4000]	[1.1, 1.1, 3.3]
D	C	[180, 360, 720]	40	50	4.0	[900, 1800, 3600]	0.25
	M	720	40	50	4.0	3600	0.25
E	C	[32, 64, 128]	50	[7, 22, 30]	5.0	[160, 320, 640]	0.20
	M	64	50	12	5.0	320	0.20
	F	64	50	18	5.0	320	0.20
F	C	200	10	20	1.0	1000	1.0
	M	200	10	20	1.0	1000	1.0
	F	200	8	20	0.8	1000	1.25

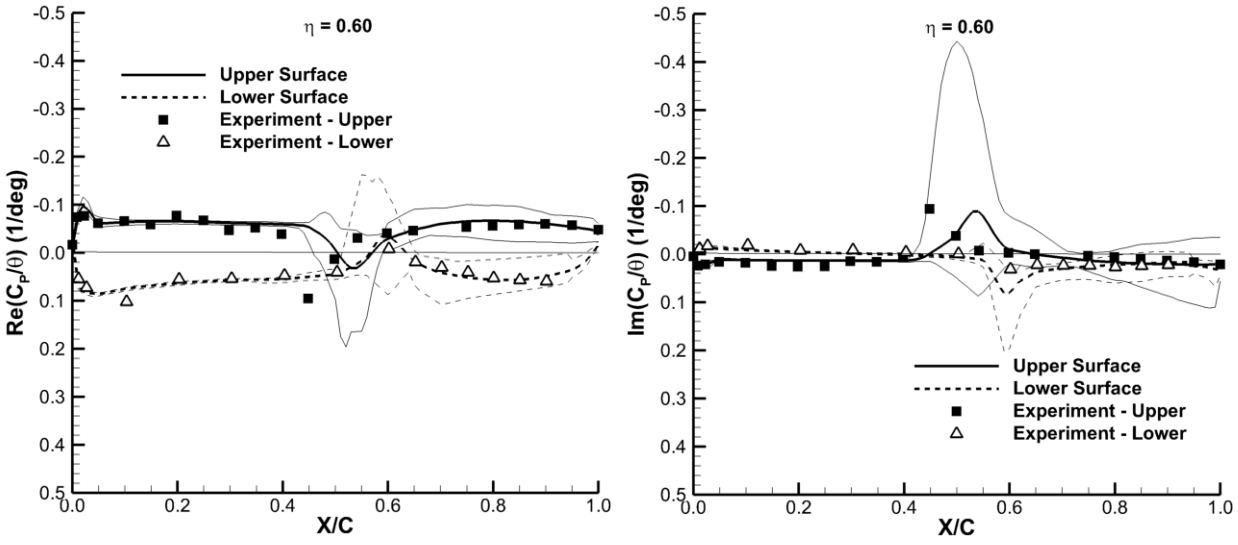

a) Real component b) Imaginary component

Figure 14. BSCW unsteady pressure comparison, M = 0.85, α = 5°, θ = 1.0°, f = 10 Hz.

The unforced cases will be reviewed first. Figure 15 shows the comparison between the AePW analyst data and the experimental data for the M = 0.70, α = 1.5°, Re_c = 7 million unforced case. The comparison between the analysis and the experiment is excellent for this subcritical case, with the largest difference seen near the leading edge of the wing at the η = 0.953 span station. The envelope surrounding the mean of the computations is nearly indistinguishable at both span stations, indicating a high degree of consistency among the analyst teams.

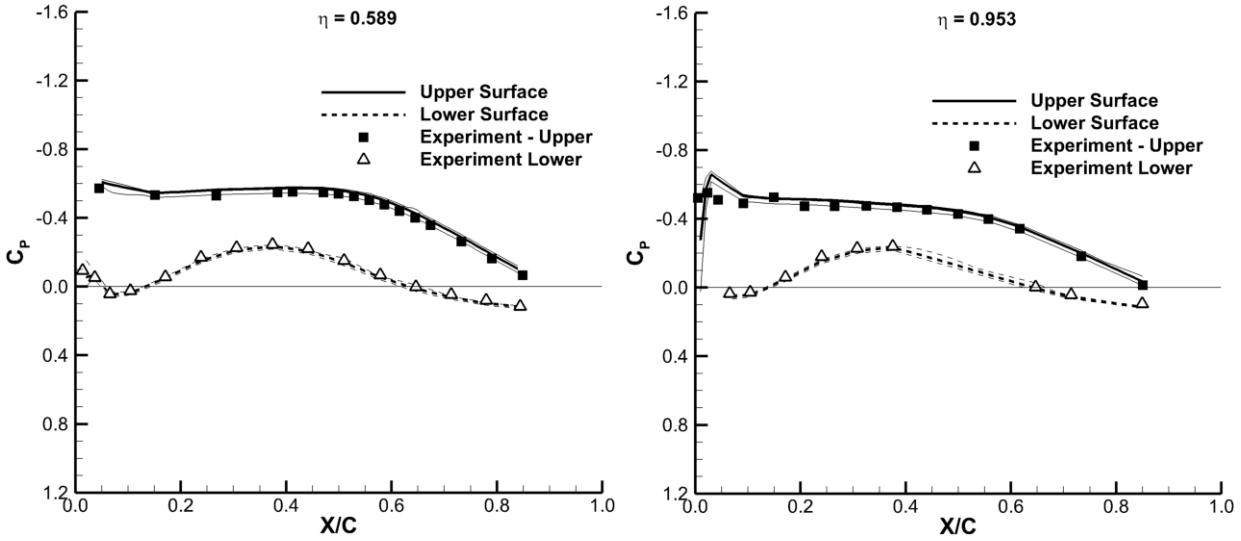

a) Inboard wing station. b) Outboard wing station.

Figure 15. HIRENASD steady pressure comparison, M = 0.70, α = 1.5°, Δz = 0.0 mm, f = 0 Hz, Re_c = 7 million.

Figure 16 presents a similar comparison for the M = 0.8, α = 1.5°, Re_c = 7 million case. For this mildly transonic case, the comparison of the average of all the computations with the experimental data is generally very good. The majority of the calculations predict the upper surface flow recompression near 50% chord at the η = 0.589 station to be slightly aft of the experimental data. The computational envelope surrounding the average is larger for this case than for the previous case, particularly near and aft of the η = 0.589, 50% chord region on the upper surface. As seen with the previous RSW and BSCW cases, the analyses begin to show larger differences as shock and other transonic nonlinearities become more prevalent. The comparison on the lower surface of the wing is very good, with the average of the computations strongly biased to one side of the envelope, indicating that the vast majority of the computations agree very closely, with only one or two outliers.

Computational and experimental data comparisons for the final unforced case at M = 0.80, α = -1.34°, and Re_c = 23.5 million are provided in Figure 17. The lower angle of attack for this case produces nearly zero net lift load on the wing and eliminates the mid-chord shock at the η = 0.589 station. The comparisons between the experimental data and the average of the computations are again very good everywhere and the calculations show very consistent results over the majority of the two stations examined. Near the leading edge of the inboard station, the envelope surrounding the computations expands in the area of the high flow acceleration on the wing lower surface.

Fluctuating pressure comparisons are shown in Figure 18 for the M = 0.70, α = 1.5°, Re = 7 million forced-oscillation case. In this example, the oscillation reference amplitude is Δz = 2.0 mm, and the frequency of oscillation is f = 79.3 Hz. The temporal parameters employed by each of the HIRENASD analysis teams are presented in Table 8. Like the unforced counterpart shown in Figure 15, the comparison between the computations and experiment is excellent for both the real and imaginary fluctuating pressure components at both wing stations. The consistency among the methods is also very good, with only minor expansion in the computational envelope near the upper-surface leading edge on the outboard station.

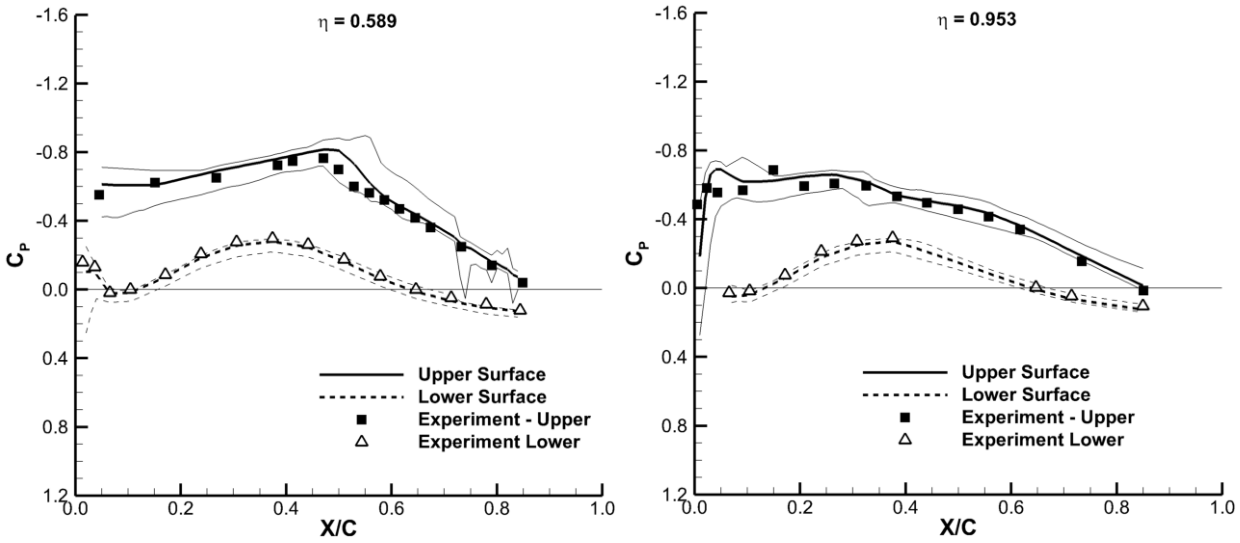

a) Inboard wing station. b) Outboard wing station.

Figure 16. HIRENASD steady pressure comparison, M = 0.80, α = 1.5°, Δz = 0.0 mm, f = 0 Hz, Re_c = 7 million.

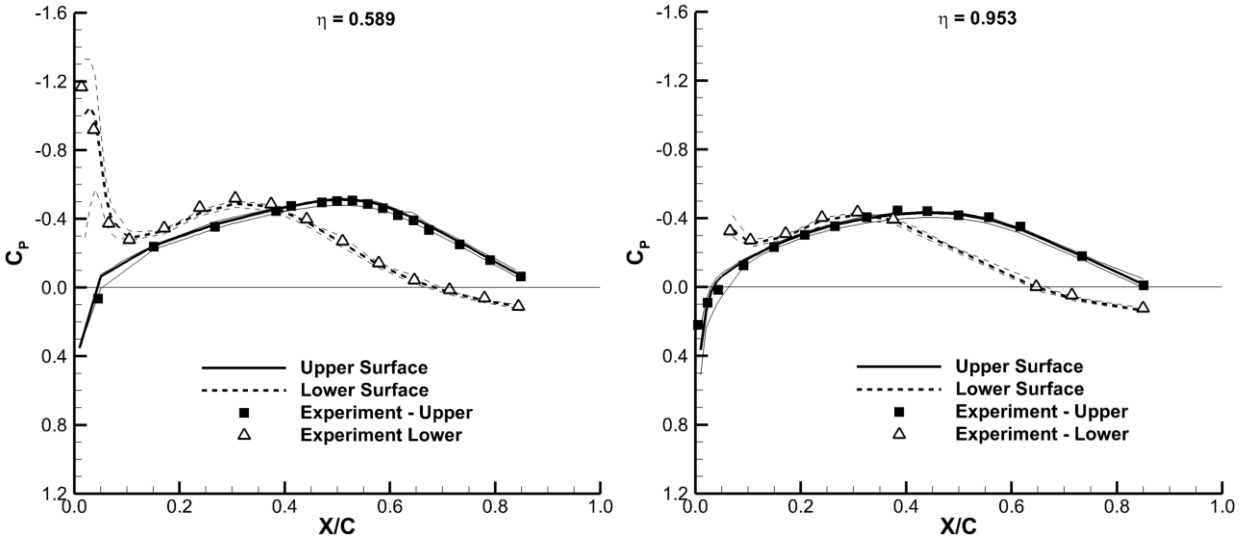

a) Inboard wing station. b) Outboard wing station.

Figure 17. HIRENASD steady pressure comparison, M = 0.80, α = -1.34°, Δz = 0.0 mm, f = 0 Hz, Re = 23.5 million.

There are a number of interesting physical characteristics that can be derived from the plots in Figure 18 that further reinforce the ability of the computational methods to accurately predict this type of aeroelastic problem. First, since the second-bending mode is being excited in this analysis and pressures are being compared at the anti-nodes of the mode, the 180° phase shift in the motion between the η = 0.589 and η = 0.953 stations can be readily observed in the pressure distributions. At these span stations under the second-bending mode, the airfoil sections are effectively undergoing a plunging motion and as a result are generating an induced local angle of attack at the wing span stations. While the tip station is moving upward and inducing a negative angle of attack, the inboard station is

moving downward and inducing a positive angle of attack, and vice versa. This is observed in the pressure distributions of Figure 18 by the swapping in orientation of the upper and lower surface pressures between the inboard and outboard stations. At the outboard station where the wing section moves up in phase with the prescribed motion, a negative induced angle of attack is generated, and the lower-surface pressures are primarily negative, while the upper surface pressures are positive. At the inboard station, the wing section moves down 180° out of phase with the upward tip motion and produces a positive induced angle of attack with the upper-surface pressures being primarily negative and lower-surface pressures primarily positive. Second, since the inboard station is nearer the wing root, the amplitude of the vertical motion at this anti-node is smaller than at the anti-node near the wing tip. Thus, the induced angle of attack inboard will be smaller than at the outboard station. This is seen in the overall smaller magnitudes of the fluctuating pressure on the inboard station versus the outboard station. Finally, there is a second, more subtle phase shift between the inboard and outboard station that is observed when examining

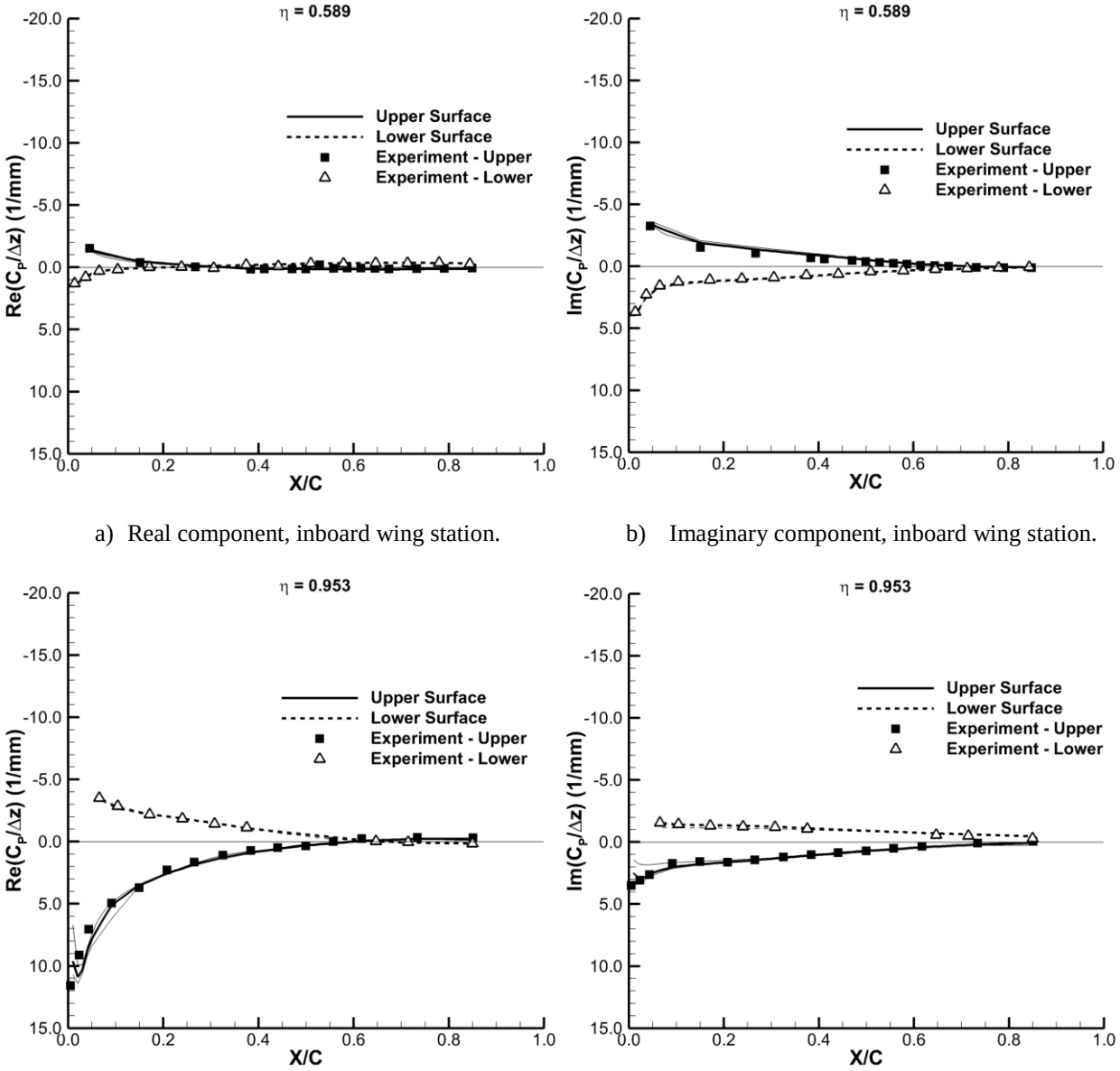

a) Real component, inboard wing station.

b) Imaginary component, inboard wing station.

c) Real component, outboard wing station.

d) Imaginary component, outboard wing station.

Figure 18. HIRENASD unsteady pressure comparison, M = 0.7, α = 1.5°, Δz = 2.0 mm, f = 79.3 Hz, Re_c = 7 million.

Table 8. HIRENASD time accurate computation parameters, M = 0.70, Re_c = 7 Million, f = 79.3 Hz.

Analyst Team	Grid Res	# of Steps per Cycle	# of Cycles Computed	# of Subiters per Global Time Step	Time Record Length (sec)	Nyquist Frequency (Hz)	Fourier Frequency Resolution (Hz)
A	M	32	4	60	0.050	2538	19.83
F	C	64	1	200	0.013	5075	79.3
	M	64	1	200	0.013	5075	79.3
	F	64	1	300	0.013	5075	79.3
G	M	64	4	50	0.050	5076	19.84
J	C	64	8	25	0.101	5075	9.91
	M	64	4	25	0.050	5075	19.82

the relative magnitudes of the real and imaginary fluctuating pressure components. At the inboard station, the imaginary component of the pressure distribution is generally larger than the real component, indicating that the inboard pressures respond nearly 90° out-of-phase with the motion of the reference sensor, which is near the wing tip. At the outboard station, however, the opposite is observed, with the real component of the pressures being generally larger than the imaginary component, which says the pressure responds nearly in-phase with the sensor motion. This second-bending mode oscillation produces a complex aerodynamic-structural interaction, the features of which are very accurately captured by the computational methods for this case.

Figure 19 shows a markedly different picture for the M = 0.80, α = 1.5°, Re_c = 7 million forced-oscillation case. The reference amplitude of oscillation for this case is Δz = 2.4 mm, and the frequency of oscillation is f = 78.9 Hz. Temporal parameters chosen for this analysis are shown in Table 9. As in the unforced case, when transonic nonlinearities are added to the computations, the predictions begin to differ substantially among each other as well as from the experimental data. For this case, the lower-surface pressures are closely predicted by most of the computations at both of the wing stations. The fact that the average and one side of the lower surface envelope are very close to the experimental data justifies this claim, with only one or two analyst submissions defining the far side of the envelope. However, the upper surface computations do not show this consistency, with a large spread in the envelope on either side of the average and across virtually the entire upper surface. There is a shock on the upper surface near 50% chord on the inboard wing station that is captured in both the experimental data and by the computations. The computational position of the shock is aft of the experimental data, as observed in the previous comparisons depicting transonic flow. At the outboard station, the upper surface average pressure comparison with the experimental data in the 10%– 40% chord region is poor, but improves beyond 40% chord. However, the envelope on both sides surrounding the average is large across the entire chord length, showing that there is a significant amount of variation among all the methods. At both stations, the general character of the upper surface pressures is captured for this case, but the differences between the computations and experiment are considered large, especially at the outboard station.

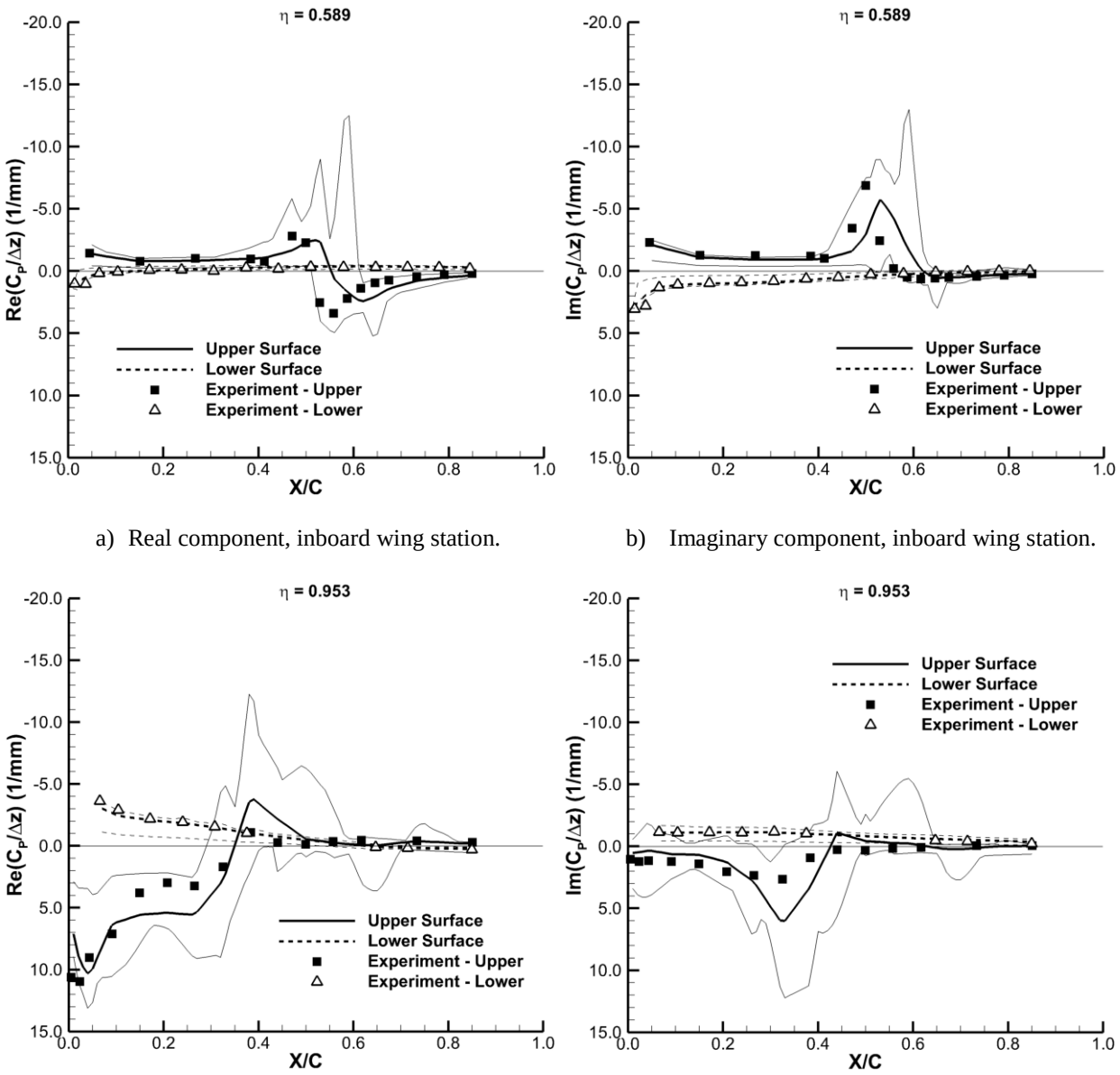

a) Real component, inboard wing station.

b) Imaginary component, inboard wing station.

c) Real component, outboard wing station.

d) Imaginary component, outboard wing station.

Figure 19. HIRENASD unsteady pressure comparison, M = 0.8, α = 1.5°, Δz = 2.4 mm, f = 78.9 Hz, Re_c = 7 million.

Table 9. HIRENASD time accurate computation parameters, M = 0.80, Re = 7 Million, f = 78.9 Hz.

Analyst Team	Grid Res	# of Steps per Cycle	# of Cycles Computed	# of Subiters per Global Time Step	Time Record Length (sec)	Nyquist Frequency (Hz)	Fourier Frequency Resolution (Hz)
A	M	32	4	60	0.051	1262	19.73
B	C	64	6	Variable	0.075	2525	13.42
C	C	100	6	15	0.076	3943	13.15
E	C	128	2	30	0.025	5050	40.0
F	C	64	1	250	0.013	2525	78.9
	M	[64, 128]	1	[250, 200]	0.013	[2525, 5050]	78.9
	F	64	1	250	0.013	2525	78.9
G	C	64	4	50	0.051	2525	19.72
H	C	64	4	25	0.051	2525	19.72
	M	64	4	25	0.051	2525	19.72
I	C	256	2	30	0.025	5000	39.45
J	C	64	8	25	0.101	2525	9.86
	M	[64, 256]	[5, 3]	25	[0.064, 0.038]	[2525, 10100]	[15.78, 26.3]
	F	64	4	25	0.051	2525	19.72
K	M	32	0	8	0.002	1262	504.96

Finally, Figure 20 compares the fluctuating pressures at M = 0.80, α = -1.34°, and Re_c = 23.5 million, with the associated temporal parameters chosen by the HIRENASD analysts presented in Table 10. The amplitude of oscillation for this case is Δz = 0.9 mm, and the frequency of oscillation is f = 80.4 Hz. The reduced mean angle of attack for this case eliminates the upper surface shock on the wing and minimizes transonic nonlinearities in the flow, except near the lower-surface leading edge. The consistency of the computations for this case is much improved over the previous case, with the largest envelope around the mean occurring near the wing leading edge. The comparison with the experimental data is also very good for this set of conditions everywhere except near the lower-surface leading edge on the inboard wing station. Even near the inboard lower-surface leading edge, however, the overall character of the real and imaginary pressure components is well-predicted, but the peak in the pressure distribution is low for all the submitted computations.

For the HIRENASD configuration, all but one of the analysts submitted their data only at the experimental pressure port locations. In high pressure gradient regions like that near the wing's outboard lower-surface leading edge, the actual computed peak pressure could occur between the experimental data points, and the peak pressure magnitude could be much larger than that portrayed in the plots. Also, a small forward or aft shift in the computed pressure peak could result in large differences at the experimental locations when the pressure gradients are very large. This is especially the case near the outboard lower-surface leading edge.

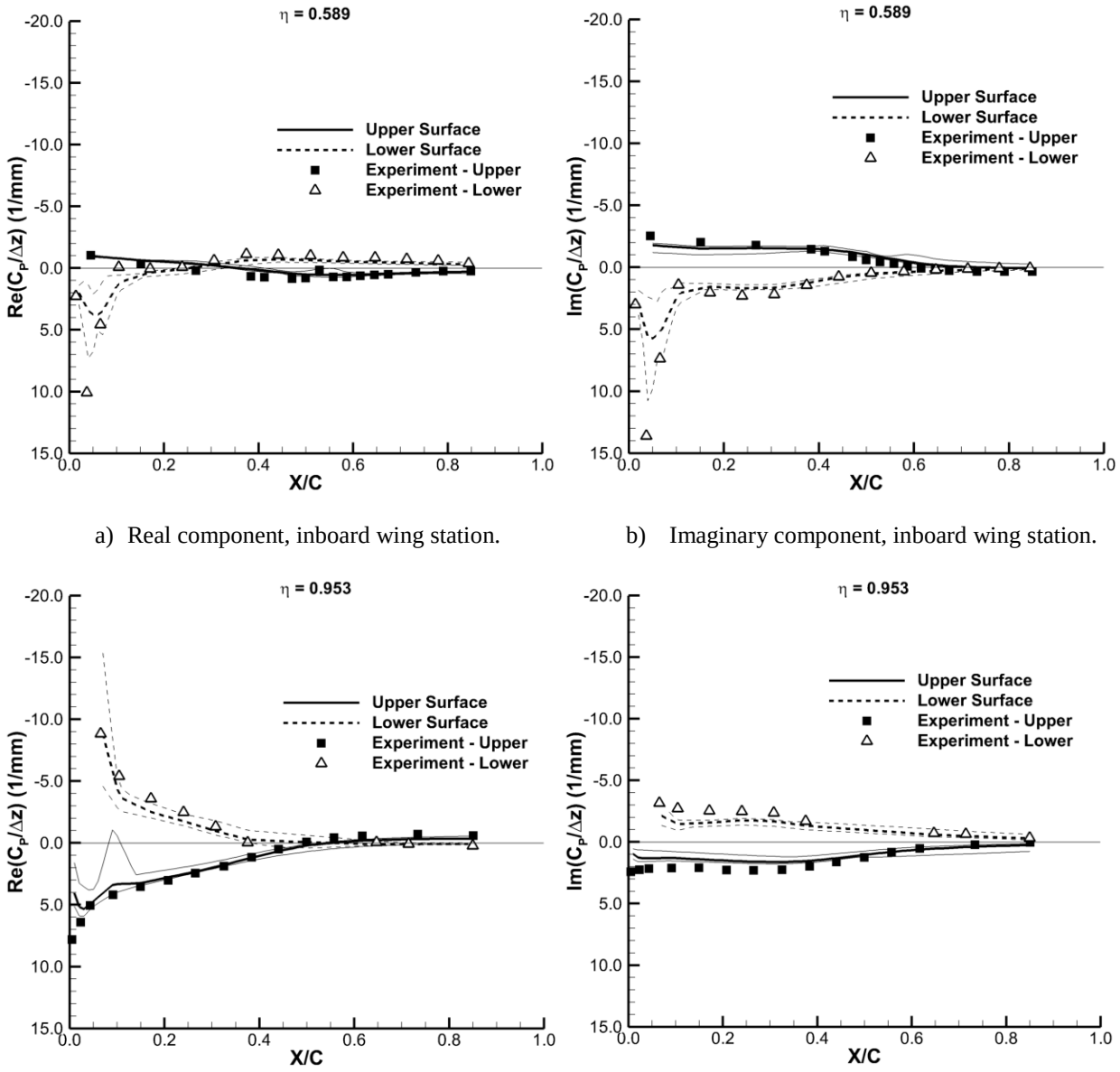

a) Real component, inboard wing station.

b) Imaginary component, inboard wing station.

c) Real component, outboard wing station.

d) Imaginary component, outboard wing station.

Figure 20. HIRENASD unsteady pressure comparison, M = 0.8, α = -1.34°, Δz = 0.9 mm, f = 80.4 Hz, Re = 23.5 million.

Table 10. HIRENASD time accurate computation parameters, M = 0.80, Re = 23.5 Million, f = 80.4 Hz.

Analyst Team	Grid Res	# of Steps per Cycle	# of Cycles Computed	# of Subiters per Global Time Step	Time Record Length (sec)	Nyquist Frequency (Hz)	Fourier Frequency Resolution (Hz)
A	M	32	4	60	0.05	1286	20
B	M	64	1	Variable	0.013	2564	79
F	C	64	1	400	0.012	2573	80
	M	[64, 128]	1	400	0.012	[2573, 5146]	80
	F	64	1	600	0.012	2573	80
G	C	64	4	50	0.05	2573	20
I	C	128	0.2	30	0.002	5146	402
J	C	64	8	25	0.1	2573	10
	M	64	4	25	0.05	2573	20
	F	64	4	25	0.05	2573	20

III. Conclusion

A thorough comparison of the unforced and foced-oscillation pressure data from computations submitted to the Aeroelastic Prediction Workshop has been performed and presented in this paper. Data from three different configurations, each with its own specific set of objectives to assess the state of the art of computational aerodynamics in predicting nonlinear unsteady aerodynamics has been collected and analyzed. The Rectangular Supercritical Wing was chosen for its geometric simplicity and relatively benign transonic flow conditions. Complexity in the experimental setup for this wing that were not recognized prior to its selection as an AePW configuration severely complicated the analysis of this wing and very likely contributed to the poor performance of the computational methods for this problem, especially at the inboard wing station. The Benchmark Supercritical Wing configuration presented a simple geometry with a set of flow conditions that were expected to be very challenging to the computational tools, and it did not disappoint. Proper grid refinement proved to be essential in performing the calculations at the static angle of attack required as the initial condition for the forced-oscillation time domain analyses. Grids that were too coarse did not exhibit the unsteady flow character that was present for this case, even though the wing was fixed at a constant angle of attack. Despite the fact that some analysts did not predict the initial unsteadiness at the fixed angle of attack, the forced-oscillation computations exhibited remarkable consistency everywhere except near and behind the shock. Variations in the computations were large in these regions and the predicted shock location was generally aft of the experiment. For both the forced and unforced computations, several analysts reported sensitivity with respect to choice of time step size, number of subiterations, and subiteration convergence. The HIRENASD configuration provided the most geometrically and mechanically complex test case, but it also provided the most consistent set of computational results and comparisons with experimental data, as long as the flow conditions were not highly transonic. The subcritical M = 0.70, α = 1.5°, Re_c = 7.0 million and M = 0.80, α = -1.34°, Re_c = 23.5 million cases showed good comparison with the experimental data and good consistency among the computations. The transonic M = 0.80, α = 1.5°, Re_c = 7.0 million case proved to be considerably more difficult for the analysts. This appears to be the general theme of the overall analyses for all the configurations. The computational methods seem to perform very well for problems and areas of the flow that are linear, but nonlinearity in the form of shock waves, shock-boundary layer interaction, flow separation, and other viscous interactions challenge both the unforced and forced-oscillation calculations. It is not clear how the accuracy of the unforced calculation used as an initial condition for the forced-oscillation analysis affects the accuracy of the forced computations, but logic says it must be a significant contributor, particularly when coupled with a structural analysis to predict static aeroelastic deformation. There is also the open question of how small errors in the initial conditions can affect the unsteady computations for highly nonlinear transonic flows. A partial answer to this question may be embedded in the data acquired for the AePW, but that analysis is beyond the scope of this paper.

The AePW analysts are continuing to refine and extend their computations and analyses for the BSCW and HIRENASD configurations. The complexity of the RSW experimental setup coupled with the age and reduced availability of the experimental data for this configuration limits its value for future analysis. The shock-buffet character of the BSCW at constant angle of attack has attracted the attention of several workshop participants who did not initially analyze this configuration and are now interested in testing their methods on it. HIRENASD has the most attractive and relevant geometry of the configurations evaluated, and it has a very large and detailed experimental database available. There were numerous test conditions and flow phenomena investigated in this experiment and it should continue to be an excellent resource for unsteady aerodynamic and aeroelastic analysis for quite some time.

Acknowledgements

This paper would not have been possible without the contributions of the analyst teams that provided computations and participated in the Aeroelastic Prediction Workshop. The authors would like to acknowledge the efforts of these teams, many of which participated on a volunteer basis. Performing these types of computations can be extremely challenging and time-consuming and it is their efforts that have enabled the success of the AePW.

References

[1]Heeg, J., et al., "Overview of the Aeroelastic Prediction Workshop," AIAA 51st Aerospace Sciences Meeting, Grapevine, TX, January 2013, (to be published).

[2]Levy, David W., et al., "Summary of Data from the First AIAA CFD Drag Prediction Workshop," AIAA Paper AIAA-2002-0841, January 2002.

[3]Rumsey, et al., "Summary of the First AIAA CFD High Lift Prediction Workshop," AIAA Paper AIAA-2011-0939, January 2011.

[4]Heeg, J., et al., "Plans for an Aeroelastic Prediction Workshop," IFASD-2011-110, International Forum on Aeroelasticity and Structural Dynamics, June 2011.

[5]Ricketts, R., et al. "Geometric and Structural Properties of a Rectangular Supercritical Wing Oscillated in Pitch for Measurement of Unsteady Pressure Distributions," NASA TM-85763, November 1983.

[6]Ricketts, R., et al., "Transonic Pressure Distributions on a Rectangular Supercritical Wing Oscillating in Pitch," NASA TM-84616, March 1983.

[7]Ricketts, R., et al., "Subsonic and Transonic Unsteady and Steady-Pressure Measurements on a Rectangular Supercritical Wing Oscillated in Pitch," NASA TM-85765, August 1984.

[8]Bennett, R. M. and Walker, C. E., "Computational Test Cases for a Rectangular Supercritical Wing Undergoing Pitching Oscillations," NASA TM-1999-209130, April 1999.

[9]Dansberry, B.E., et al., "Physical Properties of the Benchmark Models Program Supercritical Wing," NASA TM-4457, September 1993.

[10]Dansberry, B. E., "Dynamic Characteristics of a Benchmark Models Program Supercritical Wing," AIAA Paper AIAA 92-2368, April 1992.

[11]Piatak, D. J. and Cleckner, C. S., "Oscillating Turntable for the Measurement of Unsteady Aerodynamic Phenomenon," *Journal of Aircraft*, Vol. 14, No. 1, Jan. – Feb. 2003.

[12]Ballman, J., et al., "Experimental Analysis of High Reynolds Number Aero-Structural Dynamics in ETW," AIAA Paper AIAA-2008-0841, January 2008.

[13]Dafnis, A., et al. "Dynamic Response of the HiReNASD Elastic Wing Model under Wind-Off and Wind-On Conditions", International Forum on Aeroelasticity and Structural Dynamics, IF-073, 2007.

[14]Ballmann, J., et al. "Aero-structural wind tunnel experiments with elastic wing models at high Reynolds numbers (HIRENASD-ASDMAD)", AIAA Paper AIAA-2011-0882, January 2011.

[15]Reimer, L., et al., "Computational Aeroelastic Design and Analysis of the HiReNASD Wind Tunnel Wing Model and Tests," International Forum on Aeroelasticity and Structural Dynamics, IF-077, 2007.

[16]Reimer, L., Ballmann, J., and Behr, M., "Computational Analysis of High Reynolds Number Aerostructural Dynamics (HiReNASD) Experiments," IFASD-2009-132, International Forum on Aeroelasticity and Structural Dynamics, 2009.

[17]Neumann, J., and Ritter, M., "Steady and Unsteady Aeroelastic Simulations of the HIRENASD Wind Tunnel Experiment," IFASD-2009-132, International Forum on Aeroelasticity and Structural Dynamics, 2009.

[18]Neumann, J., Nitzsche, J., and Voss, R., "Aeroelastic Analysis by Coupled Non-linear Time Domain Simulation," RTO-MP_AVT-154, 2008.

[19]Wieseman, C. D., and Bennett, R. M., "Wall Boundary Layer Measurements for the NASA Langley Transonic Dynamics Tunnel," NASA TM 2007-214867, April 2007.
[20]Heeg, J., et al., "Rectangular Supercritical Wing Analyses in Support of the Aeroelastic Prediction Workshop," AIAA 51st Aerospace Sciences Meeting, Grapevine, TX, January 2013, (to be published).